Geophysical Journal International

Geophys. J. Int. (2018) **212,** 743–759
Advance Access publication 2017 October 3
GJI Marine geosciences and applied geophysics

doi: 10.1093/gji/ggx423

Rotation-induced magnetic field in a coil magnetometer generated by seismic waves

Li Jiang,[1,2] Yixian Xu,[3] Lupei Zhu,[4] Ying Liu,[1] Dehua Li[1] and Rong Huang[1]

[1] *Hubei Subsurface Multi-Scale Imaging Key Laboratory, Institute of Geophysics and Geomatics, China University of Geosciences, Wuhan, Hubei, 430074, China*
[2] *School of Mathematics and Statistics, North China University of Water Resources and Electric Power, Zhengzhou, Henan, 450046, China*
[3] *School of Earth Sciences, Zhejiang University, Hangzhou, Zhejiang, 310027, China. E-mail: xyxian@zju.edu.cn*
[4] *Department of Earth and Atmospheric Sciences, Saint Louis University, St. Louis, MO 63108, USA*

Accepted 2017 September 28. Received 2017 September 27; in original form 2017 April 30

SUMMARY

Synchronous seismic and geomagnetic fields are often observed. The magnetic field induced by seismic waves may be one of the main noises for magnetotelluric observation. Previous studies comparing the magnetic field induced by an earthquake to the estimated based on motion induction electromagnetic theory or magnetic azimuth deviation showed large differences in amplitude despite of high degree of synchronization and similarity in waveforms. According to the Faraday's principle, if a coil magnetometer takes a rotational movement in a magnetic field, the magnetic flux in the coil will be changed, generating the so-called rotation-induced magnetic field. Here we seek connection between seismic rotational motion and the rotation-induced magnetic field. The equations based on in-plane and 3-D rotational movement of a coil magnetometer caused by seismic waves passing through are derived, which permit us to predict the rotation-induced magnetic field from seismic records. As a demonstration, by using synchronous seismic and geomagnetic records observed in the Hainan Island, China, during the 2011 off the Pacific coast of Tohoku Earthquake, we successfully predicted the rotation-induced magnetic field in the periods of 5–40 s that agrees with the observed magnetic field in major characteristics including amplitude, phase, frequency, starting time and duration.

Key words: Magnetic field variations through time; Magnetotellurics; Time-series analysis; Earthquake ground motions; Rotational seismology; Wave propagation.

1 INTRODUCTION

Some studies demonstrate presence of a magnetic field disturbance associated with a strong earthquake (Nagao *et al.* 2000; Karakelian *et al.* 2002; Azeez *et al.* 2009; Starzhinskii & Nikiforov 2010; Tang *et al.* 2010; Balasco *et al.* 2014; Gao *et al.* 2014). The magnetic field disturbances cannot be easily identified in association with micro-seismicity. But the low signal-to-noise ratio (SNR) magnetic field observed in magnetotelluric (MT) signals coincides well with ambient seismic noises in the same bandwidth (∼0.2–20 s) (Egbert & Livelybrooks 1996; Sinharay & Bhattacharya 2006). The ambient seismic noises are dominated by fundamental surface waves (Barstow *et al.* 1989; Bonnefoy-Claudet *et al.* 2006; Tanimoto 2007). On the other hand, the low SNR MT signal seems to disappear for observations in desert areas (Jiang & Xu 2013) where seismic wave propagation from microseismicity and earthquakes is greatly attenuated by a thick sand layer. We thus have a reason to relate the magnetic field disturbance to seismic waves.

On the other hand, previous studies on the sources of magnetic field induced by an earthquake suggested a motion-induced electromagnetic field or by deviation of magnetic sensor's azimuth. For the first model, researchers assumed that seismic waves will deform subsurface media and thus generate motion induction effects, such as the piezoelectric (Ogawa & Utada 2000a,b; Huang 2002), the piezomagnetic (Stacey & Johnston 1972; Yamazaki 2013), the electrokinetic effects (Pride 1994; Ren *et al.* 2012; Fujinawa & Noda 2016) and the 'seismic dynamo' effects (Honkura *et al.* 2009). For the second model, they showed that the shear waves will rotate the ground and change the azimuth of magnetic sensor on the ground, which can cause observable magnetic field disturbance (Nichols *et al.* 1988; Pedersen 1988). Both models can accurately predict time and frequency but not amplitude for the magnetic disturbance. The estimated magnitudes of magnetic disturbances are usually one order or more less than the observations (Starzhinskii & Nikiforov 2010; Gao *et al.* 2014). In recent years, some scholars have supplemented some of the above theories with the much improved numerical simulation results, such as the medium effect analyses (Huang *et al.* 2015), the surface charge hypothesis (Ren *et al.* 2015) and the evanescent electromagnetic waves hypothesis

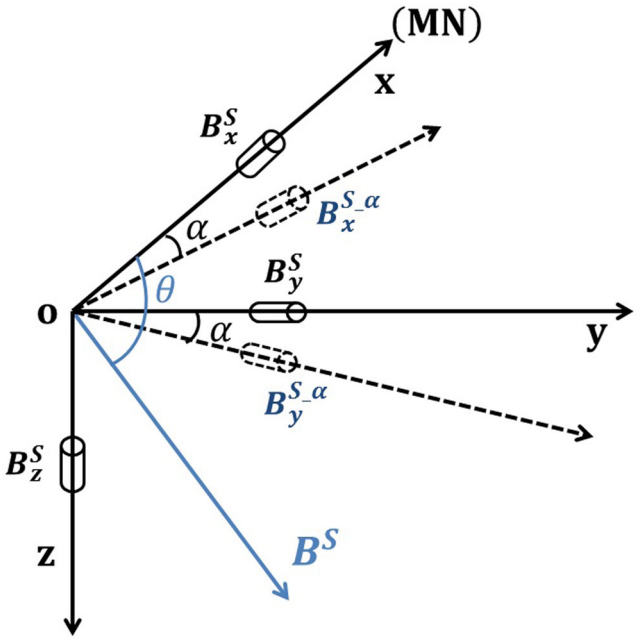

Figure 1. Conceptual model of the plane rotating induced magnetic field in a geomagnetic coordinates (MN denotes the magnetic North). Here x, y and z indicate the magnetic north, magnetic east and downward directions before xy-plane rotational movement, respectively. $\boldsymbol{B}^S$ indicates the static magnetic field whose x-, y- and z-components are B_x^S, B_y^S and B_z^S, respectively. $B_x^{S\_\alpha}$ and $B_y^{S\_\alpha}$ denote the x- and y-components of static magnetic field after xy-plane rotational movement (the rotation angle is α), and the angle θ represents geomagnetic inclination between the xy-plane and $\boldsymbol{B}^S$. Note that θ approaches zero near the geomagnetic equator and $\pm 90^\circ$ around the north and south magnetic poles, respectively.

(Ren *et al.* 2016). However, these numerical simulations do not link the actual seismic records to the actual magnetic records yet. These pioneering comparisons imply that the proposed mechanisms may not be the whole causes for the magnetic field induced by seismic waves.

Propagations of shear waves and surface waves will rotate the passing medium (Igel *et al.* 2005, 2007), which will not only generate the azimuth deviation of the deployed coil magnetometer but also force the coil cutting the lines of the static geomagnetic field (Bernardi *et al.* 1991). Taking account of the large magnitude of static geomagnetic field (about 50 μT) (Simpson & Bahr 2005), the magnetic disturbances caused by the rotational movement of a coil magnetometer in the static magnetic field cannot be ignored. If the mechanism is true, a high degree of similarity should be found in waveforms (including amplitudes) of the magnetic field disturbances and the rotational seismic component.

This study aims to building full connection between the magnetic field disturbances and rotation component of seismic waves. Based on our model, we can predict the magnetic field induced by seismic waves due to an earthquake quantitatively. The model is also validated by observations during the 2011 off the Pacific coast of Tohoku Earthquake from MT and seismic stations deployed in the Hainan island of China.

2 IN-PLANE ROTATING INDUCED MAGNETIC FIELD

Based on the principle of electromagnetic induction, the magnetic field recorded by a coil magnetometer is reflected in voltage generated by change of the magnetic flux through the coil. So the coil magnetometer senses a time-varying magnetic field instead of static magnetic field. However, if a coil magnetometer is rotating in a static magnetic field, it will sense the magnetic disturbances generated by the flux change in the coil. In order to facilitate the discussion, we call these additional time-varying magnetic disturbances as rotation-induced magnetic field (RIMF).

As shown in Fig. 1, if A^{coil} denotes the cross-sectional area of a coil magnetometer, and B^S is total strength of the static magnetic field, the primary magnetic flux Φ^{S_coil} through a coil magnetometer in three directions are

$$\begin{cases} \Phi_x^{S\_\text{coil}} = B_x^S \cdot A^{\text{coil}} = B^S \cdot A^{\text{coil}} \cdot \cos\theta, \\ \Phi_y^{S\_\text{coil}} = B_y^S \cdot A^{\text{coil}} = 0, \\ \Phi_z^{S\_\text{coil}} = B_z^S \cdot A^{\text{coil}} = B^S \cdot A^{\text{coil}} \cdot \sin\theta, \end{cases} \tag{1}$$

where the angle θ is geomagnetic inclination.

In the case of the *xy*-plane rotating around the *z*-axis by an angle α, the magnetic flux $\Phi^{S\_\alpha\_\mathrm{coil}}$ through a coil magnetometer in three directions are then

$$\begin{cases} \Phi_x^{S\_\alpha\_\mathrm{coil}} = B_x^S \cdot A^{\mathrm{coil}} \cdot \cos\alpha = B^S \cdot A^{\mathrm{coil}} \cdot \cos\theta \cdot \cos\alpha, \\ \Phi_y^{S\_\alpha\_\mathrm{coil}} = -B_x^S \cdot A^{\mathrm{coil}} \cdot \sin\alpha = -B^S \cdot A^{\mathrm{coil}} \cdot \cos\theta \cdot \sin\alpha, \\ \Phi_z^{S\_\alpha\_\mathrm{coil}} = B_z^S \cdot A^{\mathrm{coil}} = B^S \cdot A^{\mathrm{coil}} \cdot \sin\theta. \end{cases} \tag{2}$$

Comparing eqs (1) and (2), it is clear that the RIMF is present in the *x*- and *y*-components which will be recorded by a coil magnetometer.

If the rotation angular velocity changes with time (denoted as $\Omega(t)$), then the rotation angle α can be formulated as $\alpha(t) = \int_0^t \Omega_\alpha(\tau)\mathrm{d}\tau$, $(\alpha(t)|_{t=0} = 0)$. The RIMF will also be time dependent and can be written as

$$\begin{cases} B_x^{S\_\alpha}(t) = B^S \cdot \cos\theta \cdot \cos\left[\int_0^t \Omega_\alpha(\tau)\,\mathrm{d}\tau\right], \\ B_y^{S\_\alpha}(t) = -B^S \cdot \cos\theta \cdot \sin\left[\int_0^t \Omega_\alpha(\tau)\,\mathrm{d}\tau\right]. \end{cases} \tag{3}$$

Assuming that the rotation angle is very small (e.g. $|\alpha| < 0.1\,rad$), then

$$\begin{cases} \sin\alpha = \alpha + \mathrm{o}(\alpha) \approx \alpha, \\ \cos\alpha = 1 + \mathrm{o}(\alpha) \approx 1. \end{cases} \tag{4}$$

Substituting eq. (4) into eq. (3), the RIMF will be

$$\begin{cases} B_x^{S\_\alpha}(t) = B^S \cdot \cos\theta\ , \\ B_y^{S\_\alpha}(t) = -B^S \cdot \cos\theta \cdot \int_0^t \Omega_\alpha(\tau)\,d\tau\ . \end{cases} \tag{5}$$

Because a coil magnetometer cannot record a constant magnetic field, after removing the static component in eq. (5), we obtain

$$\begin{cases} B_x^{S\_rec}(t) = B_x^{S\_RIMF}(t) = 0, \\ B_y^{S\_rec}(t) = B_y^{S\_RIMF}(t) = -B^S \cdot \cos\theta \cdot \int_0^t \Omega_\alpha(\tau)\,d\tau\ . \end{cases} \tag{6}$$

Eq. (6) is the RIMF recorded by a coil magnetometer when its rotary movement in a static magnetic field is small, for example, caused by the passing seismic waves (Appendix A).

The rotational angular velocity can in general reflect the rotary movement with frequency. Supposing the rotational angular velocity changes with angular frequency ω_0 as $\Omega_\alpha(t) = A \cdot \cos(\omega_0 t)$, the RIMF can thus be written as

$$\begin{cases} B_x^{S\_RIMF}(t) = 0, \\ B_y^{S\_RIMF}(t) = -\left(\frac{1}{\omega_0}\right) A \cdot B^S \cdot \cos\theta \cdot \sin(\omega_0 t)\ . \end{cases} \tag{7}$$

Now it is clear that, by using eq. (7), the RIMF at any frequency in a rotary coil magnetometer with an angular velocity can be estimated. If the static magnetic field B^S is 50 μT, the geomagnetic inclination θ is 45°, and the amplitude of rotating angle velocity A is 10 μrad s^{-1} (or 1 μrad s^{-1}) for all frequencies, the RIMF can be estimated by using eq. (7) and shown in Fig. 2.

As clearly illustrated in Fig. 2, only the rotation-induced *y*-direction magnetic field exists. Note that its amplitudes are comparable with those of natural geomagnetic field in range of several Hertz to dozens of seconds. Fortunately, the main energy of earthquakes is also concentrated in this band, which provides convenience for the verification of RIMF. Moreover, according to eq. (7), at low geomagnetic latitudes the RIMF will be stronger due to the reduced geomagnetic inclination θ.

During the rotation of a coil magnetometer, not only the static magnetic field $\boldsymbol{B}^S$ but also the time-varying magnetic field $\boldsymbol{B}^T(t)$ can generate the RIMF. For the same model as shown in Fig. 1, the rotation-induced *z*-direction magnetic field is also zero, which is assumed to have the same direction with $\boldsymbol{B}^S$. As pointed out before, the RIMF in *y*-direction is most pronounced. To compare relative magnitudes between the RIMFs generated by static and time-varying magnetic fields, we substitute B^S with $B^T(t)$ in eq. (7) and obtain $B_y^{T\_RIMF}(t)$ generated in the time-varying magnetic field with angular velocity at angular frequency ω_0 as

$$B_y^{T\_RIMF}(t) = -\left(\frac{1}{\omega_0}\right) \cdot A \cdot B^T(t) \cdot \cos\theta \cdot \sin(\omega_0 t). \tag{8}$$

In the Fourier domain, the RIMFs generated by time-varying and static magnetic fields can be written as

$$\mathrm{B}_y^{T\_RIMF}(\omega) = \frac{\mathrm{j}}{2}\left(\frac{1}{\omega_0}\right) \cdot A \cdot \cos\theta \cdot \left[\mathrm{B}^T(\omega - \omega_0) - \mathrm{B}^T(\omega + \omega_0)\right], \tag{9}$$

$$\mathrm{B}_y^{S\_RIMF}(\omega) = \mathrm{j}\pi\left(\frac{1}{\omega_0}\right) \cdot A \cdot B^S \cdot \cos\theta \cdot [\delta(\omega - \omega_0) - \delta(\omega + \omega_0)], \tag{10}$$

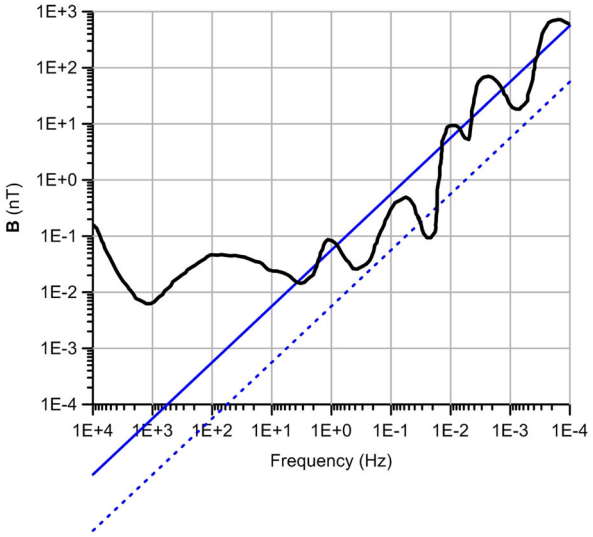

Figure 2. The estimated rotation-induced magnetic field. Black solid line indicates the spectrum of geomagnetic continuous pulsations (redraw from Kaufman & Keller 1981). According to eq. (7), assuming that B^S is 50 μT, θ is 45°, and A is 10 μrad s^{-1}, the amplitude of $B_y^{S\text{-}RIMF}$ is inversely proportional to the frequency of the rotating angular velocity (eq. 7) and denoted by blue solid lines. If we only change the amplitude of rotating angle velocity A to 1 μrad s^{-1}, the estimated $B_y^{S\text{-}RIMF}$ is plotted as blue dotted lines.

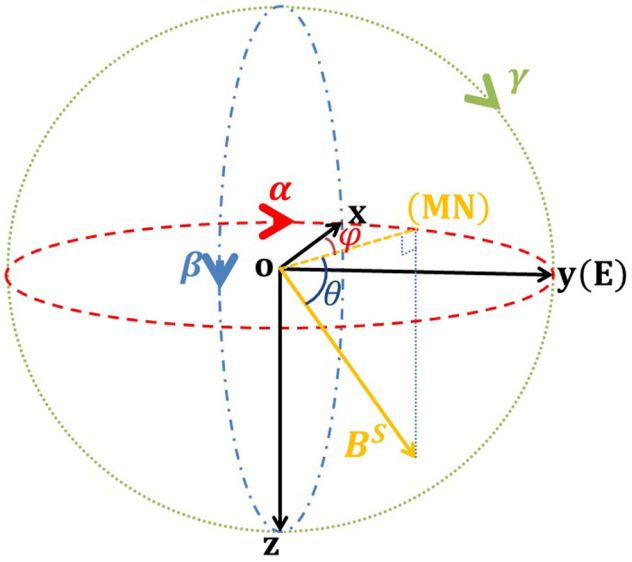

Figure 3. Model for a coil magnetometer rotating three-dimensionally in a static magnetic field $\boldsymbol{B}^S$ in a geographical coordinates. α, β and γ are the rotation angles of the xy-plane around the z-axis, the xz-plane around the y-axis and the zy-plane around the x-axis, respectively. θ is the same as in Fig. 1 and represents geomagnetic inclination, φ denotes the geomagnetic declination, and MN and E mark the magnetic north and true east, respectively.

where $\mathrm{B}(\omega) = \int_{-\infty}^{+\infty} B(t)e^{-\mathrm{j}\omega t}\mathrm{d}t$, ω and j are angular frequency and the imaginary unit, respectively. Comparing eqs (9) and (10), the ratio of RIMFs in the static magnetic field and in the time-varying magnetic field roughly equals to the ratio of their original field strengths. For a rotational angular velocity in a narrow frequency band, the conclusion is also true approximately. The static part of natural geomagnetic field is far greater than its time-varying part, so the RIMF generated by the time-varying magnetic field can be ignored.

3 3-D ROTATION-INDUCED MAGNETIC FIELD

The rotation caused by passing seismic waves, which are dominated by surface waves, is generally 3-D. We here discuss the RIMF recorded by a coil magnetometer with 3-D rotary movement in a static magnetic field. According to the model shown in Fig. 3, three components of

the static magnetic field $\boldsymbol{B}^S$ are

$$\begin{cases} B_x^S = B^S \cdot \cos\theta \cdot \cos\varphi \ , \\ B_y^S = B^S \cdot \cos\theta \cdot \sin\varphi \ , \\ B_z^S = B^S \cdot \sin\theta \ . \end{cases} \tag{11}$$

After a 3-D rotation, the magnetic fields in each direction are (Pedersen 1988)

$$\begin{bmatrix} B_x^{S\_\alpha,\beta,\gamma} \\ B_y^{S\_\alpha,\beta,\gamma} \\ B_z^{S\_\alpha,\beta,\gamma} \end{bmatrix} = \boldsymbol{R'} \begin{bmatrix} B_x^S \\ B_y^S \\ B_z^S \end{bmatrix} = \begin{bmatrix} 1 & \alpha & -\beta \\ -\alpha & 1 & \gamma \\ \beta & -\gamma & 1 \end{bmatrix} \begin{bmatrix} B_x^S \\ B_y^S \\ B_z^S \end{bmatrix}, \tag{12}$$

where $B_x^{S\_\alpha,\beta,\gamma}$, $B_y^{S\_\alpha,\beta,\gamma}$ and $B_z^{S\_\alpha,\beta,\gamma}$ are the RIMF in the x-, y- and z-directions after the 3-D rotation, respectively, and all positive rotation angles in matrix $\boldsymbol{R'}$ ($\boldsymbol{R'} = \left[\begin{smallmatrix} 1 & \alpha & -\beta \\ -\alpha & 1 & \gamma \\ \beta & -\gamma & 1 \end{smallmatrix}\right]$) (Appendix B)) are consistent with the Right-Hand Rule. Similar to implementation before, by taking account of the rotation angles changing with time and after removing the static components in eq. (12), the 3-D RIMF will be

$$\begin{bmatrix} B_x^{S\_rec}(t) \\ B_y^{S\_rec}(t) \\ B_z^{S\_rec}(t) \end{bmatrix} = \begin{bmatrix} B_x^{S\_RIMF}(t) \\ B_y^{S\_RIMF}(t) \\ B_z^{S\_RIMF}(t) \end{bmatrix} = \begin{bmatrix} 0 & \alpha(t) & -\beta(t) \\ -\alpha(t) & 0 & \gamma(t) \\ \beta(t) & -\gamma(t) & 0 \end{bmatrix} \cdot \begin{bmatrix} M \\ N \\ K \end{bmatrix} B^S, \tag{13}$$

where $M = \cos\theta \cdot \cos\varphi$. $N = \cos\theta \cdot \sin\varphi$. $K = \sin\theta$. Again, by converting the angles to the angular velocities, eq. (13) can be written as

$$\begin{bmatrix} B_x^{S\_RIMF}(t) \\ B_y^{S\_RIMF}(t) \\ B_z^{S\_RIMF}(t) \end{bmatrix} = \begin{bmatrix} 0 & \int_0^t \Omega_\alpha(\tau)\,\mathrm{d}\tau & -\int_0^t \Omega_\beta(\tau)\,\mathrm{d}\tau \\ -\int_0^t \Omega_\alpha(\tau)\,\mathrm{d}\tau & 0 & \int_0^t \Omega_\gamma(\tau)\,\mathrm{d}\tau \\ \int_0^t \Omega_\beta(\tau)\,\mathrm{d}\tau & -\int_0^t \Omega_\gamma(\tau)\,\mathrm{d}\tau & 0 \end{bmatrix} \begin{bmatrix} M \\ N \\ K \end{bmatrix} B^S, \tag{14}$$

where $\Lambda(t) = \int_0^t \Omega_\Lambda(\tau)\mathrm{d}\tau$, $\Lambda \in (\alpha, \beta, \gamma)$. If $\Omega_\beta(\tau)$ and $\Omega_\gamma(\tau)$ in eq. (14) vanish, and geomagnetic declination φ is zero (i.e. $M = \cos\theta$ and $N = 0$ in eq. 14) (Fig. 3), then the RIMF in eq. (14) is reduced to that $B_y^{S\_RIMF}(t)$ in eq. (6).

4 CONNECTING THE ROTATION-INDUCED MAGNETIC FIELD TO SEISMIC WAVES

Assuming the angular velocity vector $\boldsymbol{\Omega} = [\,\Omega^i \ \Omega^j \ \Omega^k\,]$, the linear velocity vector $\boldsymbol{V} = [\,v_x \ v_y \ v_z\,]$, and the displacement vector $\boldsymbol{U} = [\,u_x \ u_y \ u_z\,]$, and using the integral relationship $\boldsymbol{U}(t) = \int_0^t \boldsymbol{V}(\tau)\mathrm{d}\tau$ ($\boldsymbol{U}(t)|_{t=0} = 0$), the angular velocity can be represented in terms of linear velocity as

$$\boldsymbol{\Omega} = \frac{1}{2} \cdot \nabla \times \boldsymbol{V} = \frac{1}{2} \begin{bmatrix} \vec{i} & \vec{j} & \vec{k} \\ \frac{\partial}{\partial x} & \frac{\partial}{\partial y} & \frac{\partial}{\partial z} \\ v_x & v_y & v_z \end{bmatrix},$$

where $\vec{i}$, $\vec{j}$ and $\vec{k}$ are unit vectors in the positive x, y and z direction, respectively. That is

$$\begin{bmatrix} \Omega^i(t) \\ \Omega^j(t) \\ \Omega^k(t) \end{bmatrix} = \frac{1}{2} \begin{bmatrix} \frac{\partial v_z}{\partial y} - \frac{\partial v_y}{\partial z} \\ \frac{\partial v_x}{\partial z} - \frac{\partial v_z}{\partial x} \\ \frac{\partial v_y}{\partial x} - \frac{\partial v_x}{\partial y} \end{bmatrix}. \tag{15}$$

Rewriting eq. (15) by replacing the linear velocities with the displacements, that is, $\boldsymbol{V}(t) = \frac{d\boldsymbol{U}(t)}{dt} = \dot{\boldsymbol{U}}$. we obtain

$$\begin{bmatrix} \Omega^i(t) \\ \Omega^j(t) \\ \Omega^k(t) \end{bmatrix} = \frac{1}{2} \begin{bmatrix} \frac{\partial \dot{u}_z}{\partial y} - \frac{\partial \dot{u}_y}{\partial z} \\ \frac{\partial \dot{u}_x}{\partial z} - \frac{\partial \dot{u}_z}{\partial x} \\ \frac{\partial \dot{u}_y}{\partial x} - \frac{\partial \dot{u}_x}{\partial y} \end{bmatrix}. \tag{16}$$

Eq. (16) can be written in the geographical coordinates shown in Fig. 3 as

$$\begin{bmatrix} \Omega_\alpha(t) \\ \Omega_\beta(t) \\ \Omega_\gamma(t) \end{bmatrix} = \frac{1}{2} \begin{bmatrix} \frac{\partial \dot{u}_y}{\partial x} - \frac{\partial \dot{u}_x}{\partial y} \\ \frac{\partial \dot{u}_x}{\partial z} - \frac{\partial \dot{u}_z}{\partial x} \\ \frac{\partial \dot{u}_z}{\partial y} - \frac{\partial \dot{u}_y}{\partial z} \end{bmatrix} \tag{17}$$

According to eqs (14) and (17), the RIMFs can be estimated by

$$\begin{bmatrix} B_x^{S\_RIMF}(t) \\ B_y^{S\_RIMF}(t) \\ B_z^{S\_RIMF}(t) \end{bmatrix} = \frac{1}{2}\boldsymbol{R}\begin{bmatrix} M \\ N \\ K \end{bmatrix} B^S, \tag{18}$$

where matrix $\boldsymbol{R}$ ($\boldsymbol{R} = 2(\boldsymbol{R}' - \boldsymbol{I}) = 2\left[\begin{smallmatrix} 0 & \alpha & -\beta \\ -\alpha & 0 & \gamma \\ \beta & -\gamma & 0 \end{smallmatrix}\right]$) transforms the static magnetic field into RIMF by rotary movements with elements as

$$\boldsymbol{R} = \begin{bmatrix} 0 & \frac{\partial u_y}{\partial x} - \frac{\partial u_x}{\partial y} & -\frac{\partial u_x}{\partial z} + \frac{\partial u_z}{\partial x} \\ -\frac{\partial u_y}{\partial x} + \frac{\partial u_x}{\partial y} & 0 & \frac{\partial u_z}{\partial y} - \frac{\partial u_y}{\partial z} \\ \frac{\partial u_x}{\partial z} - \frac{\partial u_z}{\partial x} & -\frac{\partial u_z}{\partial y} + \frac{\partial u_y}{\partial z} & 0 \end{bmatrix}. \tag{19}$$

Considering *S*-wave propagation in the positive *x*-direction, the displacement can be decomposed into $u_y(t - \frac{x}{c})$ and $u_z(t - \frac{x}{c})$ (e.g. Shearer 2009), and the three components of *S*-wave in displacement can be written as

$$\boldsymbol{U} = \left[0\ u_y\left(t - \tfrac{x}{c}\right)\ u_z\left(t - \tfrac{x}{c}\right)\right] = \left[0\ u_y(t')\ u_z(t')\right], \tag{20}$$

where c is the *S*-wave velocity, u_z and u_y are displacements in the *z*- and *y*-directions, respectively; t and t' are the generation and arrival times of *S*-wave, respectively. Using the relationships between the displacements and particle velocities, shown in detail in Appendix C, matrix $\boldsymbol{R}$ can be rewritten as

$$\boldsymbol{R} = \frac{1}{c}\cdot\begin{bmatrix} 0 & -v_y(t') & -v_z(t') \\ v_y(t') & 0 & 0 \\ v_z(t') & 0 & 0 \end{bmatrix}, \tag{21}$$

where v_y and v_z are particle velocities in the *y*- and *z*-directions, respectively.

Substituting eq. (21) into eq. (18), the RIMF generated by *S*-wave motion is

$$\begin{bmatrix} B_x^{S\_RIMF}(t') \\ B_y^{S\_RIMF}(t') \\ B_z^{S\_RIMF}(t') \end{bmatrix} = \frac{1}{2c}\begin{bmatrix} 0 & -v_y(t') & -v_z(t') \\ v_y(t') & 0 & 0 \\ v_z(t') & 0 & 0 \end{bmatrix}\begin{bmatrix} M \\ N \\ K \end{bmatrix} B^S. \tag{22}$$

If the geomagnetic declination $\varphi = 0$, then $M = \cos\theta$, $N = 0$, and $K = \sin\theta$, eq. (22) can be simplified to

$$\begin{cases} B_x^{S\_RIMF}(t') = -\frac{1}{2c}\cdot B^S\cdot v_z(t')\cdot\sin\theta\ , \\ B_y^{S\_RIMF}(t') = \frac{1}{2c}\cdot B^S\cdot v_y(t')\cdot\cos\theta\ , \\ B_z^{S\_RIMF}(t') = \frac{1}{2c}\cdot B^S\cdot v_z(t')\cdot\cos\theta\ . \end{cases} \tag{23}$$

The radial (R) and transverse (T) directions are generally not the same as the *x*- and *y*-directions, a rotation operation is thus needed on seismic data before estimation of RIMF. Supposing the angle between the *R*-axis and the *x*-axis is ψ, as illustrated in Fig. 4, the seismic components in the propagation coordinates *RTZ* and in geomagnetic recording coordinates *xyz* can be mutually transformed by

$$\begin{bmatrix} u_x \\ u_y \\ u_z \end{bmatrix} = \begin{bmatrix} \cos\psi & \sin\psi & 0 \\ -\sin\psi & \cos\psi & 0 \\ 0 & 0 & 1 \end{bmatrix}\begin{bmatrix} u_R \\ u_T \\ u_Z \end{bmatrix} \tag{24}$$

We only focus on *S*-wave propagation, as u_R in eq. (24) does not contribute to *S*-wave, then the three-components of *S*-wave in displacement can be written as

$$\boldsymbol{U} = \left[u_T\left(t - \tfrac{r}{c}\right)\cdot\sin\psi\ u_T\left(t - \tfrac{r}{c}\right)\cdot\cos\psi\ u_Z\left(t - \tfrac{r}{c}\right)\right] = \left[u_x^S(t')\ u_y^S(t')\ u_z^S(t')\right], \tag{25}$$

where r denotes the epicentre distance of seismic station. Substituting eq. (25) into eq. (19), the rotation matrix becomes (Appendix D)

$$\boldsymbol{R} = \frac{1}{c}\begin{bmatrix} 0 & -v_T(t') & -v_Z(t')\cdot\cos\psi \\ v_T(t') & 0 & v_Z(t')\cdot\sin\psi \\ v_Z(t')\cdot\cos\psi & -v_Z(t')\cdot\sin\psi & 0 \end{bmatrix}. \tag{26}$$

Substituting eq. (26) into eq. (18), and supposing the geomagnetic declination $\varphi = 0$, the obtained RIMF is

$$\begin{cases} B_x^{S\_RIMF}(t') = -\frac{1}{2c}\cdot B^S\cdot v_Z(t')\cdot\cos\psi\cdot\sin\theta, \\ B_y^{S\_RIMF}(t') = \frac{1}{2c}\cdot B^S\cdot[v_T(t')\cdot\cos\theta + v_Z(t')\cdot\sin\psi\cdot\sin\theta], \\ B_z^{S\_RIMF}(t') = \frac{1}{2c}\cdot B^S\cdot v_Z(t')\cdot\cos\psi\cdot\cos\theta, \end{cases} \tag{27}$$

where $v_T(t')$ and $v_Z(t')$ are particle velocities for *T*- and *Z*-components, respectively.

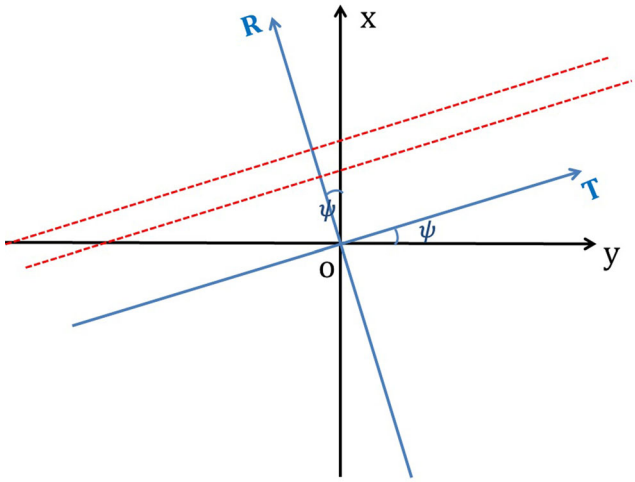

Figure 4. The coordinate rotation model of the seismic records. *RoT* are seismic wave propagation coordinates, *xoy* are seismic recording coordinates. The dotted line indicates the seismic wave front.

In terms of the *SH* and *SV* waves contained in the *T*- and *Z*-components of the seismic recordings, respectively, it is naturally to rewrite eq. (26) as

$$\boldsymbol{R} = \frac{1}{c}\begin{bmatrix} 0 & -v_{SH}(t') & -v_{SV}(t')\cdot\cos\psi \\ v_{SH}(t') & 0 & v_{SV}(t')\cdot\sin\psi \\ v_{SV}(t')\cdot\cos\psi & -v_{SV}(t')\cdot\sin\psi & 0 \end{bmatrix}, \tag{28}$$

where v_{SH} and v_{SV} are particle velocities for *SH* and *SV* waves, and are considered as the transversely polarized and vertically polarized plane waves, respectively.

For body waves, the *P*, *SV* and *SH* components can be converted from recordings in *RTZ* coordinates by the transformation (Kennett 1991; Bostock 2007)

$$\begin{bmatrix} v_P \\ v_{SV} \\ v_{SH} \end{bmatrix} = \begin{bmatrix} \frac{p\cdot\lambda^2}{\eta} & 0 & \frac{\lambda^2\cdot p^2 - 1/2}{\eta\cdot q_\eta} \\ \frac{1/2-\lambda^2\cdot p^2}{\lambda^2\cdot q_\lambda} & 0 & p\cdot\lambda \\ 0 & 1/2 & 0 \end{bmatrix} \begin{bmatrix} -v_R \\ -v_T \\ v_Z \end{bmatrix}, \tag{29}$$

where v_P is particle velocity for *P*-wave, q_η, q_λ and p are the slowness for vertical *P*, vertical *S*, and horizontal components at the surface, η and λ are the near-surface *P*- and *S*-velocities, and the wave direction is adjusted to down-going wavevetor (or point away from source) for consistency with eq. (20). Eq. (29) gives $v_{SH} = -v_T/2$, indicating that the *SH*-wave has a phase shift of π with regard to *T*-component. Substituting eqs (28) and (29) into eq. (18), the RIMF can be estimated. If again the geomagnetic declination $\varphi = 0$, the RIMF is

$$\begin{cases} B_x^{S\_RIMF}(t') = -\frac{1}{2c}\cdot B^S\cdot\xi\cdot\cos\psi\cdot\sin\theta, \\ B_y^{S\_RIMF}(t') = \frac{1}{2c}\cdot B^S\cdot\left(-\frac{1}{2}\cdot v_T(t')\cdot\cos\theta + \xi\cdot\sin\psi\cdot\sin\theta\right), \\ B_z^{S\_RIMF}(t') = \frac{1}{2c}\cdot B^S\cdot\xi\cdot\cos\psi\cdot\cos\theta. \end{cases} \tag{30}$$

where

$$\xi = -\left(\frac{\frac{1}{2}-\lambda^2\cdot p^2}{\lambda^2\cdot q_\lambda}\right)\cdot v_R(t') + p\cdot\lambda\cdot v_Z(t').$$

Surface waves (Love and Rayleigh waves) are the strongest and dominate the *T*-component and *Z*-component in seismic recordings, respectively, indicating that the RIMF is mostly generated synchronously with passing surface waves in the *T*- and *Z*-components. Following eq. (27), in association with Love and Rayleigh waves passing by, the RIMF will be approximately

$$\begin{cases} B_x^{S\_RIMF}(t') = 0, \\ B_y^{S\_RIMF}(t') = \frac{1}{2c}\cdot B^S\cdot v_T(t')\cdot\cos\theta, \\ B_z^{S\_RIMF}(t') = 0, \end{cases} \tag{31}$$

and

$$\begin{cases} B_x^{S\_RIMF}(t') = -\frac{1}{2c} \cdot B^S \cdot v_Z(t') \cdot \cos\psi \cdot \sin\theta, \\ B_y^{S\_RIMF}(t') = \frac{1}{2c} \cdot B^S \cdot v_Z(t') \cdot \sin\psi \cdot \sin\theta, \\ B_z^{S\_RIMF}(t') = \frac{1}{2c} \cdot B^S \cdot v_Z(t') \cdot \cos\psi \cdot \cos\theta, \end{cases} \tag{32}$$

respectively. It can be validated in seismic-induced magnetic field observed in Far East Russia where seismic *T*-component is closely associated with the magnetic *y*-component, and independent of the magnetic *x*- and *z*-component (Starzhinskii & Nikiforov 2010). Note that the estimations of RIMF generated by surface waves would be more accurate if taking the dispersion into account in eqs (31) and (32), which will be demonstrated in the following example.

The true North is often replaced by the magnetic North in MT and seismic observations, the magnetic declination is thus reasonably presumed to be zero in the geomagnetic coordinates, providing that the eqs (23), (27), (30), (31) and (32) can all be used for estimations of RIMF. It is worth noting that eq. (23) can only be used to estimate the magnitudes of the RIMF. Generally, accurate values of parameters in eq. (30) cannot be obtained easily, therefore eq. (27) or its derivatives of eqs (31) and (32) are suggested to be used in estimation of RIMF generated by *S* waves or surface waves passing by.

According to eqs (23), (27), (30) and (32), the ratio of $B_x^{S\_RIMF}$ to $B_z^{S\_RIMF}$ in RIMF uniquely equals to tangent of geomagnetic inclination, that is,

$$\frac{B_x^{S\_RIMF}(t)}{B_z^{S\_RIMF}(t)} = -\tan\theta. \tag{33}$$

This relation indicates that the waveforms of $B_x^{S\_RIMF}$ and $B_z^{S\_RIMF}$ are very similar, and their amplitude ratio is determined by the latitude. Obviously $B_x^{S\_RIMF}$ is greater than $B_z^{S\_RIMF}$ at high latitudes, and smaller than $B_z^{S\_RIMF}$ at low latitudes. The *x*-component of geomagnetic field recorded by a deployed coil magnetometer would be more contaminated by RIMF at high latitudes, which can be validated in seismic-induced magnetic fields observed in central China (Tang *et al.* 2010; Gao *et al.* 2014) ($\theta = 50.93^\circ$), Japan (Nagao *et al.* 2000) ($\theta = 53.9^\circ$) and Southern Italy (Balasco *et al.* 2014) ($\theta = 56.117^\circ$). On the other hand, the *z*-component would be more contaminated by RIMF at low latitudes, as observed in India (Azeez *et al.* 2009) ($\theta = 31.05^\circ$). Here all the values of geomagnetic inclination are from IGRF-12 (Thébault *et al.* 2015). The relation (eq. 33) supplies an effective tool to check the correctness of the estimated RIMF. In addition, as shown in Fig. 3, the geomagnetic inclination θ is positive in the northern hemisphere, implying that the waveforms of $B_x^{S\_RIMF}$ and $B_z^{S\_RIMF}$ are completely opposite phase. For an example illustrated in Nagao *et al.* (2000), the B_x and B_z are very similar but phase reversal in the magnetic fields recorded at (39.88°N, 140.93°E).

5 EXAMPLE OF ROTATION-INDUCED MAGNETIC FIELD

As pointed out before, one can estimate the RIMF from seismic records by using one of the eqs (23), (27) and (30) for shear waves and eqs (31) and (32) for surface waves. Fortunately we have three synchronous three-component seismic and two five-component MT stations in the Hainan Island (Fig. 5), China, which recorded the 2011 off the Pacific coast of Tohoku Earthquake. According to the US Geological Survey (http://earthquake.usgs.gov/earthquakes/eqinthenews/2011/usc0001xgp/#details), the earthquake took place on March 11, 2011, 05:46:24 (UTC), at the epicentre of (38.297°N, 142.372°E). As shown in Fig. 5, relative to the epicentre and seismic stations BSL, QZN and WZS are located basically along a great circle; the distances of QZN and WZS to BSL are about 58 and 100 km, respectively. The MT sites are marked as SP and S40, and S40 is a remote referencing site and about 43 km south to SP. QZN and SP are very close, separated by about 15 km.

Because seismic station QZN and MT station SP are very close, we will focus on their waveforms from the earthquake. At first it is worth noting that a bandpass filter is specified by (T1, T2, T3, T4), where (T2, T3) is the pass band, (T1, T2) and (T3, T4) are the transition bands (or skirts), respectively. It is obvious that no similarity exists in the waveforms of original magnetic fields at SP (Fig. 6a) and seismic records at QZN (Fig. 6b). However, significant similarity of their waveforms actually exists during the time of UTC 06:03:00 to 06:12:00 (Figs 6c and d), when the records have been bandpass (1, 5, 40, 55 s) filtered (Appendix F). As aforementioned and described in eqs (31) and (32), the Love waves dominate the T-component and only contribute to the *y*-component of RIMF, and the Rayleigh waves dominate the Z-component and contribute to all the three components of RIMF. Moreover, according to the distance (3801 km) between the epicentre and QZN and previously estimated phase velocity (3.77 ± 0.04 km s^{-1}) of Rayleigh waves for this earthquake (Hao *et al.* 2013), it is easily determined that the shear and surface waves dominate the teleseismic records during the time of 05:59:00 to 06:13:00. The features and previous studies provide us an opportunity to check accuracy of the RIMFs estimated from seismic rotary movement by using the formulations derived before.

According to the 3-D rotation model (Fig. 3), the geomagnetic inclination θ is 26.15°, the geomagnetic declination φ is 0° (*x*-direction of the coil magnetometer layouts precisely point to the magnetic north, and true declination is −1.433°), and the magnetic induction intensity of static magnetic field B^S is 43.8 μT at QZN (from IGRF-12 at that day). The angle ψ between seismic propagation direction *R* and the true north is 131.12° which is calculated by gpsCalc (http://www.pc6.com//softview/SoftView_96 462.html).

According to the results given by Shen *et al.* (2016), in Hainan Island the *S*- and Rayleigh-wave velocities in the period of 10–20 s are about 3.67 and 3.3 km s^{-1}, and the corresponding Love-wave velocity is estimated around 3.45 km s^{-1}. In the following calculations we thus use the *S*-wave velocity of 3.67 km s^{-1} for seismic series before UTC 06:05:00, and the Love- and Rayleigh-wave velocities of 3.45 km s^{-1}

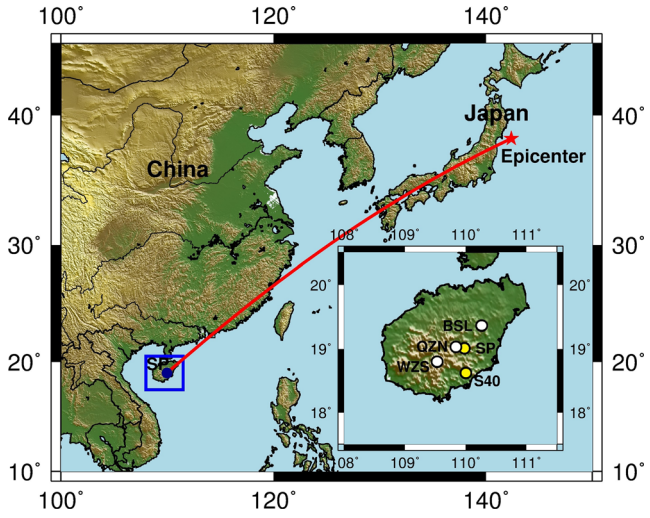

Figure 5. Locations of the 2011 off the Pacific coast of Tohoku Earthquake (the epicenter denoted by red star), and used three permanent seismic stations (inset with white solid circles) and two deployed MT sites (inset with yellow solid circles). The three seismic stations are BSL (19.3633°N, 110.2616°E), QZN (19.03°N, 109.84°E) and WZS (18.7972°N, 109.5276°E), and two deployed MT sites are SP (19.009075°N, 109.977775°E) and S40 (18.621183°N,110.001769°E). WZS, QZN and BSL to the epicenter are about 3843, 3801 and 3744 km, respectively; the distances of MT sites S40 and SP to the epicenter are about 3819 and 3792 km, respectively.

and 3.3 km s^{-1} for seismic *T*- and *Z*-components after UTC 06:05:00, respectively. The $B_x^{S\_RIMF}$, $B_y^{S\_RIMF}$ and $B_z^{S\_RIMF}$ estimated from the seismic data (Fig. 6d) by using eq. (27) or (30) are shown in Fig. 7.

Clearly the RIMF estimated from eq. (27) shows obvious similarity in waveform to the observed magnetic field components (Figs 7a, b and d). The $B_z^{S\_RIMF}$ (Fig. 7d) shows relatively better fit than that of $B_x^{S\_RIMF}$ (Fig. 7a) and $B_y^{S\_RIMF}$ (Fig. 7b). As the explanation given for eq. (33), the feature matches well with the theoretical prediction for an observation deployed in low latitude areas. We also mentioned that, although the estimated $B_y^{S\_RIMF}$ by using eq. (27) (Fig. 7b) is consistent with magnetic records in frequency, there are significant differences between the amplitudes and phases in the UTC 06:02:30–06:08:30 for the *T*- component (Fig. 6d). Compared with magnetic records, the amplitude of the estimated $B_y^{S\_RIMF}$ is larger, and their phase is opposite during the time, therefore, the accurate *SH* waves instead of *T*-component should be used to estimate the $B_y^{S\_RIMF}$. The estimations can be improved by using the eq. (30), particularly for shear waves dominated seismic sequences (Fig. 7c). Please note that $\xi \approx v_Z(t')$ in eq. (30), because the estimated $B_z^{S\_RIMF}$ by eq. (27) is basically correct. Moreover, comparing to the observed magnetic component, the significant phase delays for the estimated $B_y^{S\_RIMF}$ can be observed in surface waves dominated time-series (the strongest energies in seismic recordings), implying the seismic velocity dispersion should be taken into account in accurate estimation of RIMF.

Note that the $B_y^{S\_RIMF}$ is associated with the seismic *T*- and *Z*-components (eqs 27 and 30), and the phase velocities of Love and Rayleigh waves can be unchanged approximately in a narrow band. The dispersive characteristics can be seen in time–distance plot as shown in Fig. 8 in which the estimated RIMFs at BSL and WZS and geomagnetic fields recorded at S40 are also portrayed.

The most prominent wave train at periods of 5 to 40 s possesses visible dispersion, coinciding with the Rayleigh waves in the seismic Z-component (Fig. 8a). The feature becomes distinguishable in the dominant periods of 15–19 s for the same wave train, as shown in Fig. 8(b). The estimated phase velocity of Rayleigh waves from Fig. 8(b) is almost the same as 3.3 km s^{-1} by Shen *et al.* (2016). For the narrow-band (12, 15, 19, 25 s) filtered seismic recordings (Appendix F), we can get almost perfect estimations of RIMF at QZN station (Fig. 9).

6 DISCUSSION AND CONCLUSIONS

Through formula derivation and a real demonstration, we suggest that the RIMF is part of observation anomaly generated by rotational movement of a coil magnetometer in response to shear and surface waves passing by. In the example shown above, though the estimated RIMFs are close to the observations in waveforms, some differences cannot be ignored yet. These differences can be caused by many factors. Regardless of the stations QZN and SP are not deployed at the same site, inaccurate parameters used in eq. (30) and velocity dispersion also prevent accurate estimation of RIMF. Of course, if the frequency dependent seismic velocity can be used, the estimated results will be improved. In addition, we have no tool to separate the RIMF directly from the seismic-induced magnetic fields for comparing with the estimated RIMF. Finally we need to bear in mind that all the derived equations are based on assumption of small rotational movement generated by seismic waves propagations, which is valid in general (Appendix A). The instrument to measure Earth's true arbitrary rotation has not been available (Igel *et al.* 2005; Igel *et al.* 2007), which prevents us from further investigation of RIMF uniquely at present. Moreover, the RIMF induced by the time-varying magnetic field is commonly minor, however, if the product of spectral amplitude and bandwidth of

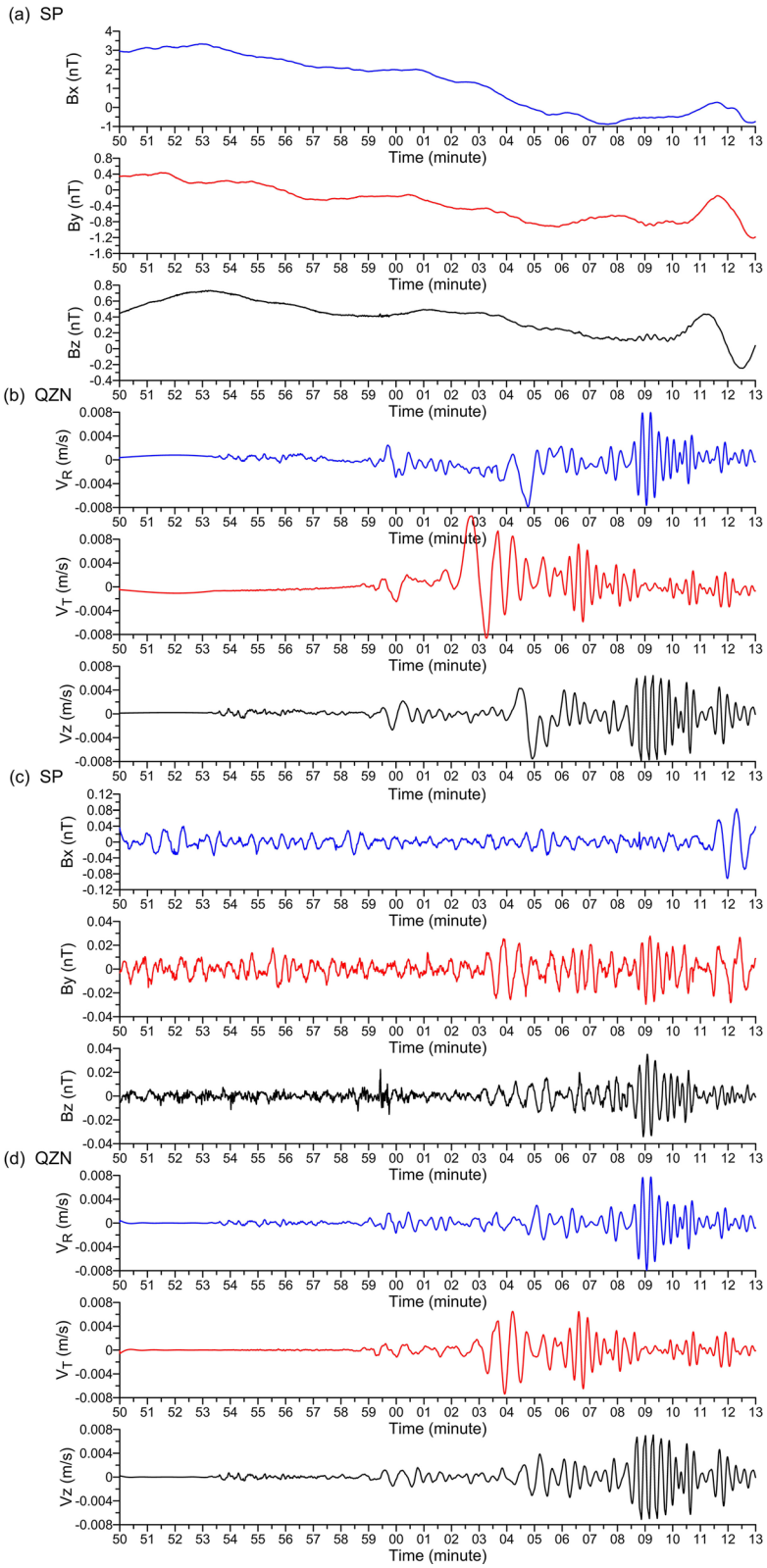

Figure 6. Time-series with the start time at 2011 March 11, 05:50:00 (UTC), and lasting 23 min for (a) original three-component magnetic fields records at SP (Appendix E), (b) original three-component seismic records at QZN, (c,d) the time-series in (a) and (b) after bandpass (1, 5, 40, 55 s) filtered. All records have the same sampling rate 4 Hz.

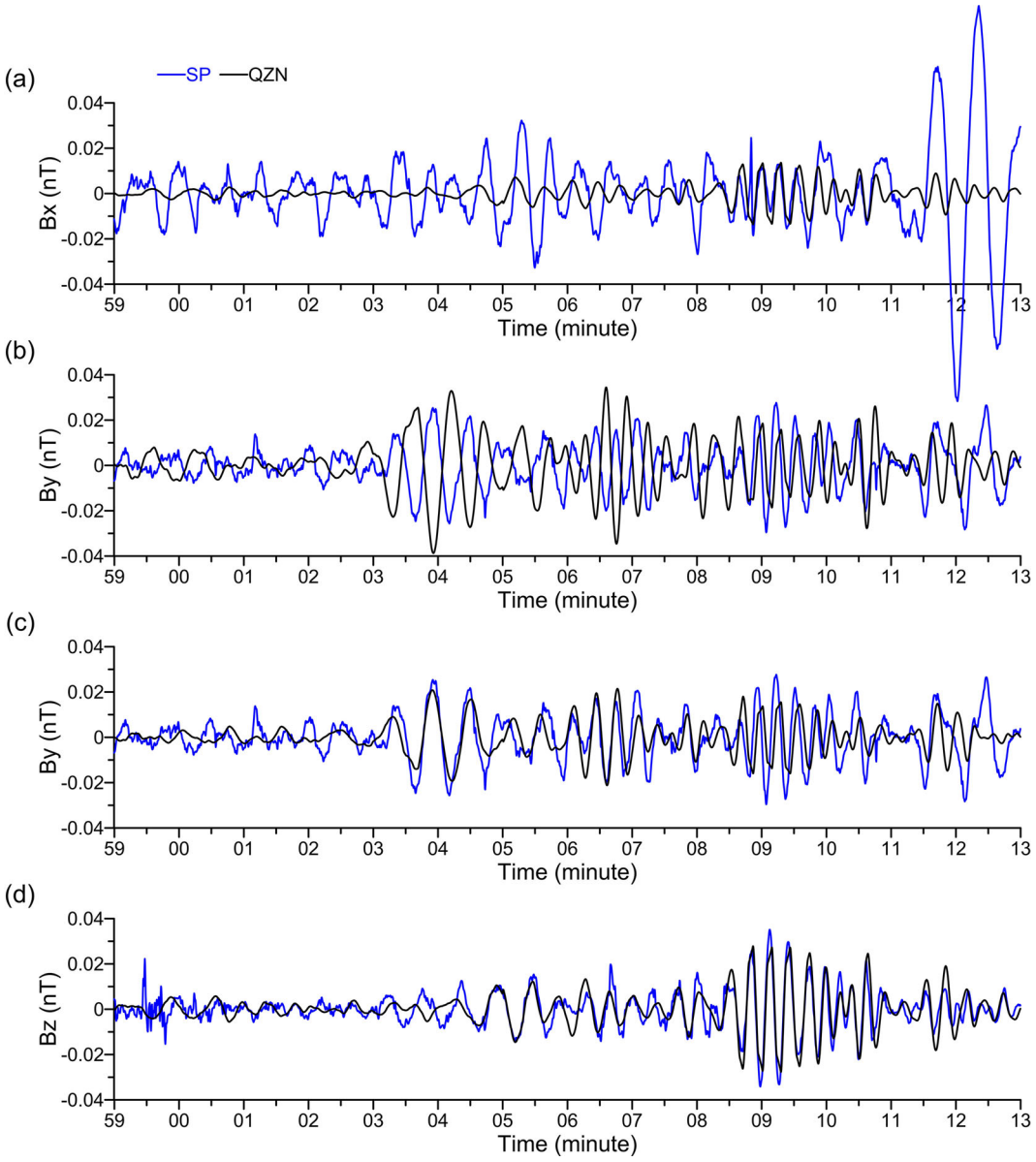

Figure 7. Waveform comparisons between the observed magnetic components (blue solid line) at SP (Fig. 6c) and the estimated RIMF (black solid line) from the seismic observations at QZN (Fig. 6d). (a) $B_x^{S\text{-}RIMF}$, (b) $B_y^{S\text{-}RIMF}$ and (d) $B_z^{S\text{-}RIMF}$, estimated from eq. (27) by using *S*-wave phase velocity of 3.67 km s^{-1}, Love-wave phase velocity of 3.45 km s^{-1} and Rayleigh-wave phase velocity of 3.3 km s^{-1}; (c) $B_y^{S\text{-}RIMF}$ estimated from eq. (30) by using the above phase velocities. Note that the arrival-time difference of seismic waves between QZN and SP is about 2.5 s (calculated from separation difference to the epicentre ∼9 km and phase velocity of 3.67 km s^{-1}) and has been compensated in the calculations.

the rotational angular velocity of a coil magnetometer is close to 1, the RIMF induced by the time-varying magnetic field cannot be ignored (Appendix G).

Compared to other models as summarized in the introduction, the present model of RIMF can predict the amplitudes of seismic-induced magnetic fields with high accuracy. From the test of a real-world example given before, the good matches between observations of magnetic field and estimated RIMF suggest that (1) the RIMF generated in a coil magnetometer are very likely to be one of the main sources of the seismic-induced magnetic field, (2) the formulations for estimation of RIMF are basically correct and (3) narrow-band filtering can be used to improve the RIMF estimation particularly for surface waves dominated seismic series (Appendix F).

ACKNOWLEDGEMENTS

We are grateful for supports from National Science Foundation of China (41530319 and 41374079) and SinoProbe-01–03. We are particularly grateful to professor Gary Egbert (AE) and two anonymous reviewers for their constructive comments and improvement of the draft. The data for this paper are available by contacting the corresponding author at xyxian@zju.edu.cn.

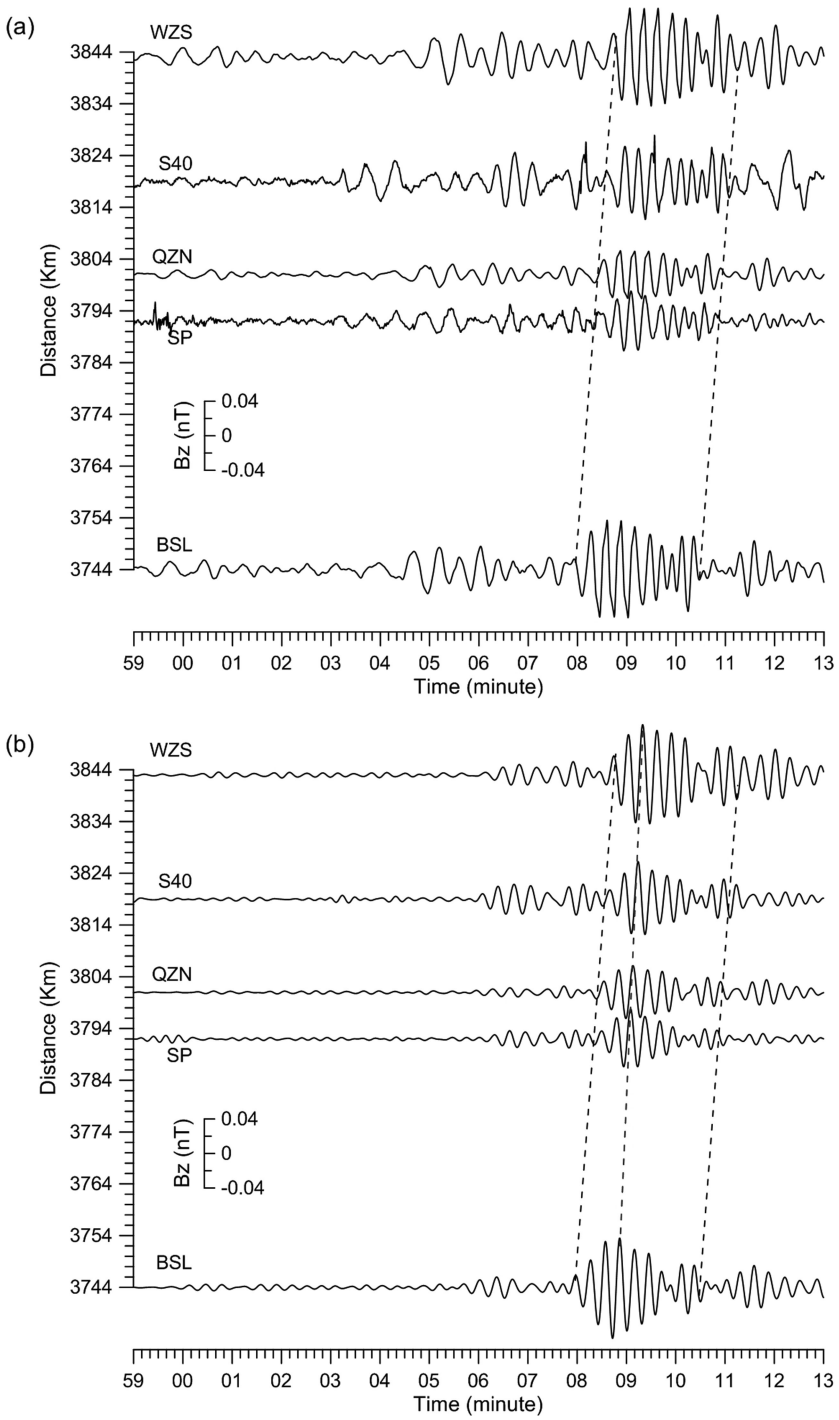

Figure 8. Time–distance (relative to the epicentre) plot of *z*-components in geomagnetic fields recorded at SP and S40 (e.g. black solid line in Fig. 5c) and in the estimated RIMFs at three seismic stations (e.g. black solid line in Fig. 7d). All data have been bandpass (1, 5, 40, 55 s) filtered in (a) and narrow-band (12, 15, 19, 25 s) filtered in (b). It is clear that the most prominent wave train, corresponding to the Rayleigh waves in Fig. 6(d), shows the dispersive characteristics. The phase velocity of Rayleigh waves in narrow-band (b), as indicated by the gradient of blue dashed line, is slightly larger than the group velocity which is indicated by the gradient of two-parallel black dashed lines.

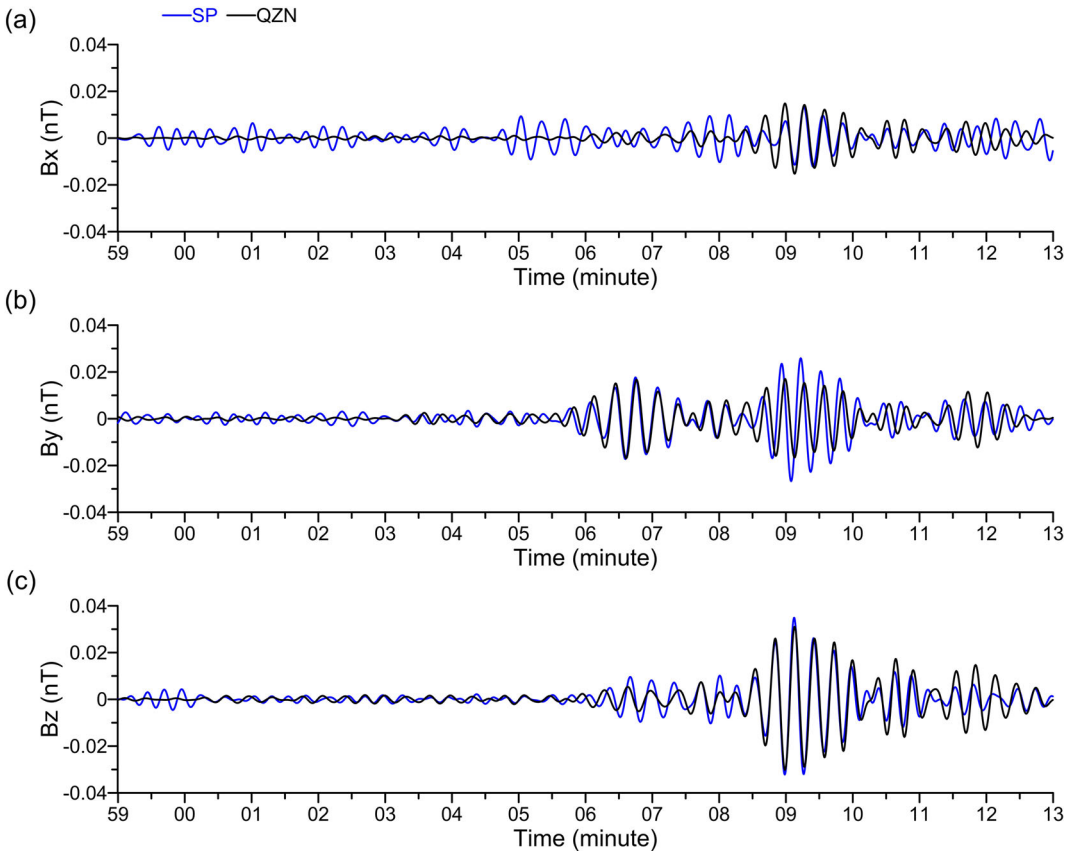

Figure 9. Improved estimations of RIMF at QZN station, where all recordings are narrow-band (12, 15, 19, 25 s) filtered.

REFERENCES

Azeez, K.K.A., Manoj, C., Veeraswamy, K. & Harinarayana, T., 2009. Co-seismic EM signals in magnetotelluric measurement—a case study during Bhuj earthquake (26th January 2001), India, *Earth Planets Space,* **61**(8), 973–981.

Balasco, M., Lapenna, V., Romano, G., Siniscalchi, A., Stabile, T.A. & Telesca, L., 2014. Electric and magnetic field changes observed during a seismic swarm in Pollino Area (southern Italy), *Bull. seism. Soc. Am.,* **104**(3), 1289–1298.

Barstow, N., Sutton, G.H. & Carter, J.A., 1989. Particle motion and pressure relationships of ocean bottom noise: 3900 m depth; 0.003 to 0.05 Hz, *Geophys. Res. Lett.,* **16**(10), 1185–1188.

Bernardi, A., Fraser-Smith, A.C., McGill, P.R. & Villard, O.G., Jr., 1991. ULF magnetic field measurements near the epicenter of the Ms 7.1 Loma Prieta earthquake, *Phys. Earth planet. Inter.,* **68,** 45–63.

Bonnefoy-Claudet, S., Cotton, F. & Bard, P.Y., 2006. The nature of noise wavefield and its applications for site effects studies: a literature review, *Earth-Sci. Rev.,* **79**(3–4), 205–227.

Bostock, M.G., 2007. Teleseismic body-wave scattering and receiver-side structure, in *Treatise on Geophysics,* vol. 1, pp. 219–246, Seismology and the Structure of the Earth, ed. Schubert, G., Elsevier.

Egbert, G.D. & Livelybrooks, D.W., 1996. Single station magnetotelluric impedance estimation: coherence weighting and the regression m-estimate, *Geophysics,* **61**(4), 964–970.

Fujinawa, Y. & Noda, Y., 2016. Characteristics of seismoelectric wave fields associated with natural microcracks. *Pure appl. Geophys.,* **173**(1), 1–14.

Gao, Y., Chen, X., Hu, H., Wen, J., Tang, J. & Fang, G., 2014. Induced electromagnetic field by seismic waves in earth's magnetic field, *J. geophys. Res.,* **119**(7), 5651–5685.

Hao, Y.Q., Xiao, Z. & Zhang, D.H., 2013. Teleseismic magnetic effects (TMDs) of 2011 tohoku earthquake, *J. geophys. Res.,* **118**(6), 3914–3923.

Honkura, Y., Ogawa, Y., Matsushima, M., Nagaoka, S., Ujihara, N. & Yamawaki, T., 2009. A model for observed circular polarized electric fields coincident with the passage of large seismic waves, *J. geophys. Res.,* **114,** B10103, doi:10.1029/2008JB006117.

Huang, Q., 2002. One possible generation mechanism of co-seismic electric signals, *Proc. Japan Acad. B,* **78**(7), 173–178.

Huang, Q., Ren, H., Dan, Z. & Chen, Y.J., 2015. Medium effect on the characteristics of the coupled seismic and electromagnetic signals, *Proc. Japan Acad. B,* **91**(1), 17–24.

Igel, H., Schreiber, U., Flaws, A., Schuberth, B., Velikoseltsev, A. & Cochard, A., 2005. Rotational motions induced by the M 8.1 Tokachi-Oki earthquake, September 25, 2003, *Geophys. Res. Lett.,* **32**(8), 93–114.

Igel, H., Cochard, A., Wassermann, J., Flaws, A., Schreiber, U., Velikoseltsev, A. & Dinh, N.P., 2007. Broad-band observations of earthquake-induced rotational ground motions, *Geophys. J. Int.,* **168**(1), 182–196.

Jiang, L. & Xu, Y.X., 2013. Multi-station superposition for magnetotelluric signal, *Stud. Geophys. Geod.,* **57**(2), 276–291.

Karakelian, D., Beroza, G.C., Klempere, S.L. & Fraser-Smith, A.C., 2002. Analysis of ultralow-frequency electromagnetic field measurements associated with the 1999 M 7.1 Hector Mine, California, earthquake sequence, *Bull. seism. Soc. Am.,* **92**(4), 1513–1524.

Kaufman, A.A. & Keller, G.V., 1981. *The Magnetotelluric Sounding Method,* Elsevier Science Press.

Kennett, B.L.N., 1991. The removal of free surface interactions from three-component seismograms, *Geophys. J. Int.,* **104,** 153–163.

Matzander, U., 2009. *MFS-06e Product Manual,* Metronix Measurement Instruments and Electronics Ltd.

Nagao, T., Orihara, Y., Yamaguchi, T., Takahashi, I., Hattori, K., Noda, Y., Sayanagi, K. & Uyeda, S., 2000. Coseismic geoelectric potential changes observed in Japan, *Geophys. Res. Lett.,* **27**(10), 1535–1538.

Nichols, E.A., Morrison, H.F. & Clarke, J., 1988. Signals and noise in measurements of low-frequency geomagnetic fields, *J. geophys. Res.,* **93**(B11), 13 743–13 754.

Ogawa, T. & Utada, H., 2000a. Electromagnetic signals related to incidence of a teleseismic body wave into a subsurface piezoelectric body, *Earth Planets Space,* **52**(4), 253–260.

Ogawa, T. & Utada, H., 2000b. Coseismic piezoelectric effects due to a dislocation: 1. An analytic far and early-time field solution in a homogeneous whole space, *Phys. Earth planet. Inter.,* **121**(s 3–4), 273–288.

Pedersen, L.B., 1988. Some aspects of magnetotelluric field procedures, *Surv. Geophys.,* **9**(3–4), 245–257.

Pride, S., 1994. Governing equations for the coupled electromagnetics and acoustics of porous media, *Phys. Rev. B,* **50**(21), 15 678–15 696.

Ren, H., Chen, X. & Huang, Q., 2012. Numerical simulation of coseismic electromagnetic fields associated with seismic waves due to finite faulting in porous media, *Geophys. J. Int.,* **188**(3), 925–944.

Ren, H., Wen, J., Huang, Q. & Chen, X., 2015. Electrokinetic effect combined with surface-charge assumption: a possible generation mechanism of coseismic EM signals, *Geophys. J. Int.,* **200**(2), 835–848.

Ren, H., Huang, Q. & Chen, X., 2016. Existence of evanescent electromagnetic waves resulting from seismoelectric conversion at a solid–porous interface, *Geophys. J. Int.,* **204**(1), 147–166.

Shearer, P., 2009. *Introduction to Seismology,* 2nd edn, Cambridge Univ. Press.

Shen, W. *et al.*, 2016. A seismic reference model for the crust and uppermost mantle beneath China from surface wave dispersion, *Geophys. J. Int.,* **206**(2), 954–979.

Simpson, F. & Bahr, K., 2005. *Practical Magnetotellurics,* Cambridge Univ. Press.

Sinharay, R.K. & Bhattacharya, B.B., 2006. Remote reference magnetotelluric impedance estimation of wideband data using hybrid algorithm, *J. geophys. Res.,* **111**(B11), 335–360.

Stacey, F.D. & Johnston, M.J.S., 1972. Theory of the piezomagnetic effect in titanomagnetite-bearing rock, *Pure appl. Geophys.,* **97**(1), 146–155.

Starzhinskii, S.S. & Nikiforov, V.M., 2010. Analysis of the magnetometer response to the passage of seismic wave, *Izv. Phys. Solid Earth,* **46**(2), 154–164.

Tang, J., Zhan, Y., Wang, L.F., Dong, Z.Y. & Zhao, G.Z., 2010. Electromagnetic coseismic effect associated with aftershock of Wenchuan Ms 8.0 earthquake, *Chin. J. Geophys.,* **53**(3), 526–534.

Tanimoto, T., 2007. Excitation of microseisms, *Geophys. Res. Lett.,* **34,** L05308, doi:10.1029/2006GL029046.

Thébault, E. *et al.*, 2015. International geomagnetic reference field: the 12th generation. *Earth Planets Space,* **67,** 79, doi:10.1186/s40623-015-0228-9.

Yamazaki, K., 2013. Improved models of the piezomagnetic field for the 2011 Mw 9.0 Tohoku-Oki earthquake, *Earth planet. Sci. Lett.,* **363**(2), 9–15.

APPENDIX A: SMALL ROTATIONAL ANGLE CAUSED BY THE SEISMIC WAVES

The Taylor series expansions for cosine and sine functions respectively are:

$$\sin\alpha = \alpha - \frac{\alpha^3}{3!} + \frac{\alpha^5}{5!} - \cdots = \alpha + \mathrm{o}(\alpha), \tag{A1}$$

$$\cos\alpha = 1 - \frac{\alpha^2}{2!} + \frac{\alpha^4}{4!} - \cdots = 1 + \mathrm{o}(\alpha), \tag{A2}$$

So, if the expansions are truncated at second derivative, the absolute deviations (Δ) and relative errors (δ) will be

$$\Delta_{\sin\alpha} = \frac{\alpha^3}{3!} + \mathrm{o}\left(\alpha^3\right), \tag{A3}$$

$$\Delta_{\cos\alpha} = \frac{\alpha^2}{2!} + \mathrm{o}\left(\alpha^2\right), \tag{A4}$$

$$\delta_{\sin\alpha} = \frac{\Delta_{\sin\alpha}}{\alpha + \mathrm{o}(\alpha)} = \frac{\alpha^2}{3!} + \mathrm{o}\left(\alpha^2\right), \tag{A5}$$

$$\delta_{\cos\alpha} = \frac{\Delta_{\cos\alpha}}{1 + \mathrm{o}(\alpha)} = \frac{\alpha^2}{2!} + \mathrm{o}\left(\alpha^2\right). \tag{A6}$$

When α is small (e.g. $|\alpha| < 0.1$ rad), $|\delta_{\sin\alpha}| < 1.7 \times 10^{-3}$, $|\delta_{\cos\alpha}| < 5 \times 10^{-3}$.

For *SH*-wave propagation, the rotational angular velocity $\Omega_\alpha(t)$ is (Igel *et al.* 2005)

$$\Omega_\alpha(t) = \frac{1}{2}\left(\frac{\partial v_y}{\partial x} - \frac{\partial v_x}{\partial y}\right) = \frac{1}{2} v_0 \cdot \cos\left[\omega_0\left(t - \frac{x}{c}\right)\right] \cdot \left(-\frac{\omega_0}{c}\right), \tag{A7}$$

where the mass point oscillation velocity $v_y(t - \frac{x}{c}) = v_0 \cdot \sin[\omega_0(t - \frac{x}{c})]$, v_0 represents the oscillation rate at x; ω_0 and c are angular frequency and propagation velocity of *SH*-wave, respectively; t and x are propagation time and distance, respectively. Then the rotation angle α can be formulated as

$$\alpha(t) = \int_0^t \Omega_\alpha(\tau)\,\mathrm{d}\tau = \frac{1}{2} v_0 \cdot \sin\left[\omega_0\left(t - \frac{x}{c}\right)\right] \cdot \left(-\frac{1}{c}\right). \tag{A8}$$

Supposing $max\{|\alpha(t)|\} < 0.1 \Rightarrow \frac{v_0}{2c} < 0.1 \Rightarrow v_0 < 0.2c$, we can immediately get $|\delta_{\sin\alpha}| < 1.7 \times 10^{-3}$, $|\delta_{\cos\alpha}| < 5 \times 10^{-3}$. The condition of $v_0 < 0.2c$ is easily matched in practice.

APPENDIX B: MATRIX R' IN EQ. (12)

According to Fig. 3 and eq. (4), rotation matrices around x-axis with angle γ, around y-axis with angle β, and around z-axis with angle α, are respectively obtained as

$$\begin{pmatrix} 1 & 0 & 0 \\ 0 & 1 & \gamma \\ 0 & -\gamma & 1 \end{pmatrix}, \quad \begin{pmatrix} 1 & 0 & -\beta \\ 0 & 1 & 0 \\ \beta & 0 & 1 \end{pmatrix}, \text{ and } \begin{pmatrix} 1 & \alpha & 0 \\ -\alpha & 1 & 0 \\ 0 & 0 & 1 \end{pmatrix}.$$

Multiplication of these three matrices expresses rotation in three-direction as

$$\begin{pmatrix} 1 & 0 & 0 \\ 0 & 1 & \gamma \\ 0 & -\gamma & 1 \end{pmatrix} \begin{pmatrix} 1 & 0 & -\beta \\ 0 & 1 & 0 \\ \beta & 0 & 1 \end{pmatrix} \begin{pmatrix} 1 & \alpha & 0 \\ -\alpha & 1 & 0 \\ 0 & 0 & 1 \end{pmatrix} = \begin{pmatrix} 1 & \alpha & -\beta \\ -\alpha+\beta\gamma & 1+\alpha\beta\gamma & \gamma \\ \beta+\alpha\gamma & -\gamma+\alpha\beta & 1 \end{pmatrix}. \tag{B1}$$

By neglecting terms of second or more order of angles α, β and γ, the matrix $\boldsymbol{R}'$ can be obtained

$$\boldsymbol{R}' = \begin{bmatrix} 1 & \alpha & -\beta \\ -\alpha & 1 & \gamma \\ \beta & -\gamma & 1 \end{bmatrix}. \tag{B2}$$

In general, different order of matrices multiplication leads to a different matrix, but neglect of higher order terms results in the same matrix, $\boldsymbol{R}'$.

APPENDIX C: MATRIX R FOR THE SHEAR WAVE RECORDS IN VELOCITY

Substituting eq. (20) into eq. (19), the partial derivatives of elements in matrix $\boldsymbol{R}$ are as follows.

$$\frac{\partial u_y}{\partial x} = \frac{\partial u_y\left(t-\frac{x}{c}\right)}{\partial x} = -\frac{1}{c}\cdot\frac{\partial u_y\left(t-\frac{x}{c}\right)}{\partial t} = -\frac{1}{c}\cdot v_y\left(t-\frac{x}{c}\right), \tag{C1}$$

$$\frac{\partial u_z}{\partial x} = \frac{\partial u_z\left(t-\frac{x}{c}\right)}{\partial x} = -\frac{1}{c}\cdot\frac{\partial u_z\left(t-\frac{x}{c}\right)}{\partial t} = -\frac{1}{c}\cdot v_z\left(t-\frac{x}{c}\right). \tag{C2}$$

The partial derivatives of the other elements are zeros. Substituting eqs (C1) and (C2) into eq. (19), the matrix $\boldsymbol{R}$ can be written as

$$\boldsymbol{R} = \frac{1}{c}\cdot\begin{bmatrix} 0 & -v_y\left(t-\frac{x}{c}\right) & -v_z\left(t-\frac{x}{c}\right) \\ v_y\left(t-\frac{x}{c}\right) & 0 & 0 \\ v_z\left(t-\frac{x}{c}\right) & 0 & 0 \end{bmatrix}. \tag{C3}$$

Eq. (21) can be obtained by variable substitution ($t' = t - \frac{x}{c}$) in eq. (C3).

APPENDIX D: MATRIX R IN EQ. (26)

According to the coordinate model shown in Fig. 4, the distance $r = \cos\psi\cdot x - \sin\psi\cdot y$ in eq. (25). Substituting eq. (25) into eq. (19), the partial derivatives of elements in matrix $\boldsymbol{R}$ are as follows.

$$\frac{\partial u_x}{\partial y} = \frac{\partial\left[u_T\left(t-\frac{\cos\psi\cdot x-\sin\psi\cdot y}{c}\right)\cdot\sin\psi\right]}{\partial y} = \frac{sin\psi}{\mathrm{c}}\cdot\frac{\partial\left[u_T\left(t-\frac{\cos\psi\cdot x-\sin\psi\cdot y}{c}\right)\cdot\sin\psi\right]}{\partial t} = \frac{\sin^2\psi}{\mathrm{c}}\cdot\frac{\partial u_T(t')}{\partial t} = \frac{\sin^2\psi}{\mathrm{c}}\cdot v_T\left(t'\right), \tag{D1}$$

$$\frac{\partial u_y}{\partial x} = \frac{\partial\left[u_T\left(t-\frac{\cos\psi\cdot x-\sin\psi\cdot y}{c}\right)\cdot\cos\psi\right]}{\partial x} = -\frac{\cos\psi}{\mathrm{c}}\cdot\frac{\partial\left[u_T\left(t-\frac{\cos\psi\cdot x-\sin\psi\cdot y}{c}\right)\cdot\cos\psi\right]}{\partial t} = -\frac{\cos^2\psi}{c}\cdot\frac{\partial u_T(t')}{\partial t} = -\frac{\cos^2\psi}{c}\cdot v_T\left(t'\right), \tag{D2}$$

$$\frac{\partial u_z}{\partial x} = \frac{\partial\left[u_Z\left(t-\frac{\cos\psi\cdot x-\sin\psi\cdot y}{c}\right)\right]}{\partial x} = -\frac{\cos\psi}{\mathrm{c}}\cdot\frac{\partial\left[u_Z\left(t-\frac{\cos\psi\cdot x-\sin\psi\cdot y}{c}\right)\right]}{\partial t} = -\frac{\cos\psi}{c}\cdot\frac{\partial u_Z(t')}{\partial t} = -\frac{\cos\psi}{c}\cdot v_Z\left(t'\right), \tag{D3}$$

$$\frac{\partial u_z}{\partial y} = \frac{\partial\left[u_Z\left(t-\frac{\cos\psi\cdot x-\sin\psi\cdot y}{c}\right)\right]}{\partial y} = \frac{\sin\psi}{\mathrm{c}}\cdot\frac{\partial\left[u_Z\left(t-\frac{\cos\psi\cdot x-\sin\psi\cdot y}{c}\right)\right]}{\partial t} = \frac{\sin\psi}{\mathrm{c}}\cdot\frac{\partial u_Z(t')}{\partial t} = \frac{\sin\psi}{\mathrm{c}}\cdot v_Z\left(t'\right), \tag{D4}$$

$$\frac{\partial u_x}{\partial z} = \frac{\partial u_y}{\partial z} = 0, \tag{D5}$$

where $t' = t - \frac{\cos\psi\cdot x-\sin\psi\cdot y}{c}$. Substituting eqs (D1) to (D5) into eq. (19), the matrix $\boldsymbol{R}$ can be written as eq. (26).

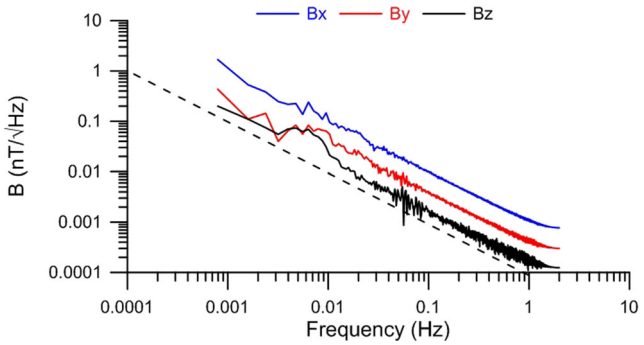

Figure E1. Spectrum of original three-component magnetic fields records at SP shown in Fig. 6(a). The blue, red and black lines are the spectrum densities of B_x, B_y and B_z in Fig. 6(a), respectively. The black dotted line marks the equivalent magnetic field noise of the coil magnetometer deployed at SP, where the magnetometer is MFS-06e with noise level given by Metronix (Matzander 2009).

APPENDIX E: THE SENSITIVITY OF THE COIL MAGNETOMETER

In frequency domain, the spectrum densities of B_x, B_y and B_z are basically higher than the sensor's noise (Figure E1). In time domain, the amplitude of RIMFs can reach about 0.04 nT (as seen in Fig. 8) in periods of dozens of seconds, which can be reliably measured by the sensor.

APPENDIX F: FILTER PARAMETERS

As shown in Fig. F1(a), the power spectral densities of geomagnetic records increase roughly linearly with period. It can be seen from Fig. F1(b) that the dominant power spectral densities of seismic records appear in the period longer than 12 s. According to eq. (27) (or eqs 31 and 32), $B_x^{S\_RIMF}$ and $B_z^{S\_RIMF}$ are only related to the *Z*- component of seismic records, but $B_y^{S\_RIMF}$ is related to the *Z*- and *T*- component of the seismic records. Therefore, the ratio of the power spectral density of the seismic to the corresponding geomagnetic record can roughly estimate the relative intensity ratio of the RIMF to background magnetic field. Figs F1(c), (d) and (e) show the ratio of the relative intensity of the RIMFs to background magnetic field in *x*-, *y*- and *z*-component, respectively; the ratio for $B_z^{S\_RIMF}$ is most remarkable (Fig. F1e), followed for the ratio for $B_y^{S\_RIMF}$ (Fig. F1d) and the ratio for $B_x^{S\_RIMF}$ is minor (Fig. F1c).

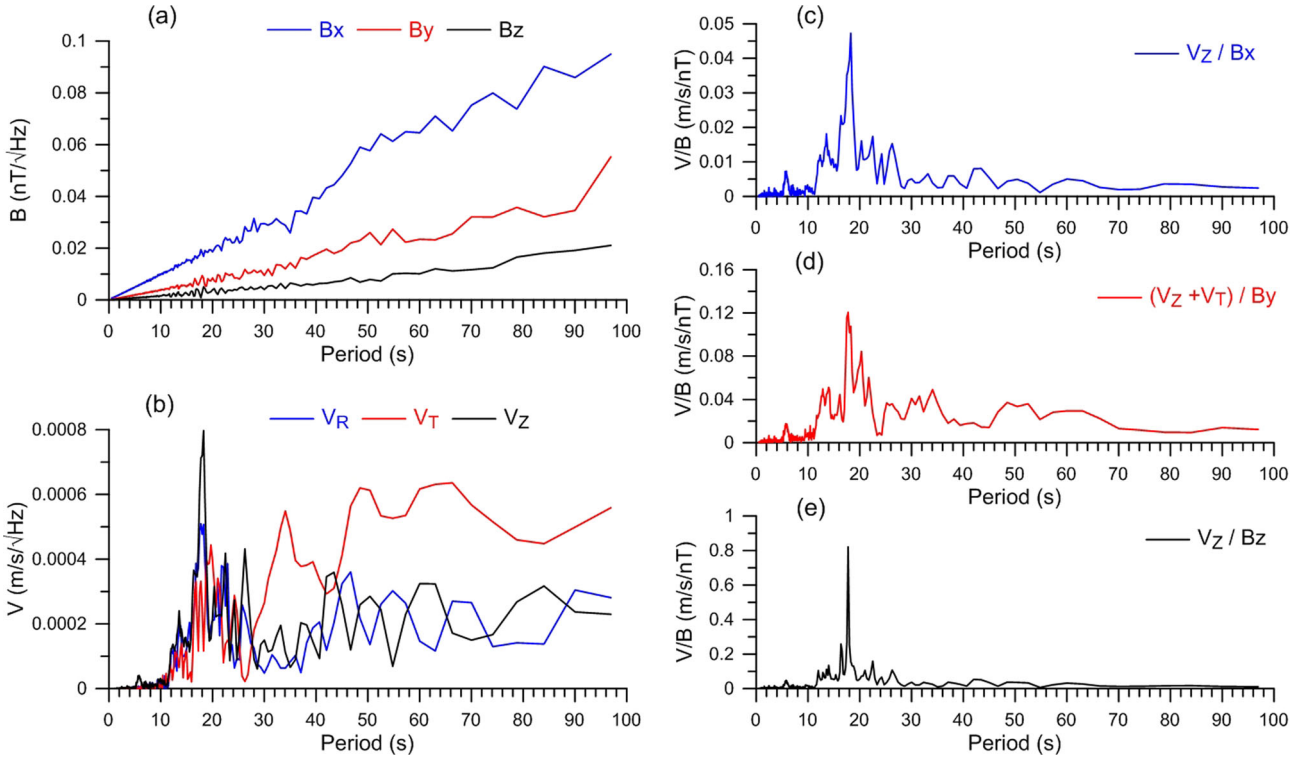

Figure F1. The power spectral densities for the seismic and geomagnetic records shown in Fig. 6: (a) the power spectral densities of original magnetic records at SP in Fig. 6(a), (b) the power spectral densities of original seismic records at QZN in Fig. 6(b), (c) the ratio of power spectral density of V_Z to B_x, (d) the ratio of power spectral density of the sum of V_Z and V_T to B_y and (e) the ratio of power spectral density of V_Z to B_z.

According to Figs F1(c), (d) and (e), the RIMFs are the most prominent in the period near 18 s, and beyond the range of 5–40 s, the RIMFs will be difficult to highlight. Therefore, the initial bandpass filter is set to (1, 5, 40, 55 s). If the filter is set to (12, 15, 19, 25 s), the RIMFs can be further highlighted.

APPENDIX G: RIMF INDUCED BY THE TIME-VARYING MAGNETIC FIELD

According to eq. (12), the RIMF induced by the time-varying magnetic field is

$$\begin{bmatrix} B_x^{T\_\alpha,\beta,\gamma}(t) \\ B_y^{T\_\alpha,\beta,\gamma}(t) \\ B_z^{T\_\alpha,\beta,\gamma}(t) \end{bmatrix} = \begin{bmatrix} B_x^{T\_rec}(t) \\ B_y^{T\_rec}(t) \\ B_z^{T\_rec}(t) \end{bmatrix} = \begin{bmatrix} 1 & \alpha(t) & -\beta(t) \\ -\alpha(t) & 1 & \gamma(t) \\ \beta(t) & -\gamma(t) & 1 \end{bmatrix} \begin{bmatrix} B_x^T(t) \\ B_y^T(t) \\ B_z^T(t) \end{bmatrix}, \tag{G1}$$

where $B_x^T(t)$, $B_y^T(t)$ and $B_z^T(t)$ are the three components of the true magnetic field, and $B_x^{T\_rec}(t)$, $B_y^{T\_rec}(t)$ and $B_z^{T\_rec}(t)$ are the three components of magnetic records by a coil magnetometer. The angles are converted to the angular velocity in rotation matrix in eq. (G1), one can obtain

$$\begin{bmatrix} B_x^{T\_rec}(t) \\ B_y^{T\_rec}(t) \\ B_z^{T\_rec}(t) \end{bmatrix} = \begin{bmatrix} 1 & \int_0^t \Omega_\alpha(\tau)\,\mathrm{d}\tau & -\int_0^t \Omega_\beta(\tau)\,\mathrm{d}\tau \\ -\int_0^t \Omega_\alpha(\tau)\,\mathrm{d}\tau & 1 & \int_0^t \Omega_\gamma(\tau)\,\mathrm{d}\tau \\ \int_0^t \Omega_\beta(\tau)\,\mathrm{d}\tau & -\int_0^t \Omega_\gamma(\tau)\,\mathrm{d}\tau & 1 \end{bmatrix} \begin{bmatrix} B_x^T(t) \\ B_y^T(t) \\ B_z^T(t) \end{bmatrix}. \tag{G2}$$

Converting eq. (G2) to frequency domain, one can obtain

$$\begin{aligned} \begin{bmatrix} \mathrm{B}_x^{T\_rec}(\omega) \\ \mathrm{B}_y^{T\_rec}(\omega) \\ \mathrm{B}_z^{T\_rec}(\omega) \end{bmatrix} &= \frac{1}{2\pi \cdot \mathrm{j}\omega} \begin{bmatrix} 2\pi \cdot \delta(\omega) \cdot \mathrm{j}\omega & \Omega_\alpha(\omega) & -\Omega_\beta(\omega) \\ -\Omega_\alpha(\omega) & 2\pi \cdot \delta(\omega) \cdot \mathrm{j}\omega & \Omega_\gamma(\omega) \\ \Omega_\beta(\omega) & -\Omega_\gamma(\omega) & 2\pi \cdot \delta(\omega) \cdot \mathrm{j}\omega \end{bmatrix} * \begin{bmatrix} \mathrm{B}_x^T(\omega) \\ \mathrm{B}_y^T(\omega) \\ \mathrm{B}_z^T(\omega) \end{bmatrix} \\ &= \begin{bmatrix} \mathrm{B}_x^T(\omega) \\ \mathrm{B}_y^T(\omega) \\ \mathrm{B}_z^T(\omega) \end{bmatrix} + \frac{1}{2\pi \cdot j\omega} \begin{bmatrix} 0 & \Omega_\alpha(\omega) & -\Omega_\beta(\omega) \\ -\Omega_\alpha(\omega) & 0 & \Omega_\gamma(\omega) \\ \Omega_\beta(\omega) & -\Omega_\gamma(\omega) & 0 \end{bmatrix} * \begin{bmatrix} \mathrm{B}_x^T(\omega) \\ \mathrm{B}_y^T(\omega) \\ \mathrm{B}_z^T(\omega) \end{bmatrix} \\ &= \begin{bmatrix} \mathrm{B}_x^T(\omega) \\ \mathrm{B}_y^T(\omega) \\ \mathrm{B}_z^T(\omega) \end{bmatrix} + \begin{bmatrix} \mathrm{B}_x^{T\_RIMF}(\omega) \\ \mathrm{B}_y^{T\_RIMF}(\omega) \\ \mathrm{B}_z^{T\_RIMF}(\omega) \end{bmatrix}. \end{aligned} \tag{G3}$$

where the $*$ denotes convolution.

The second term of the second equality in eq. (G3) represents the RIMF induced by time-varying magnetic field. In terms of the convolution rule and the wideband natural magnetic field, if the product of amplitude and bandwidth of the angular velocity spectrum is close to 1, the magnitude of the RIMF will be close to that of the time-varying magnetic field itself, hinting the significant RIMF will be presented.